



Spiral dynamics in pattern-forming systems: mean-flow effects

Lev S. Tsimring¹

Institute for Nonlinear Science, University of California at San Diego, La Jolla, CA 92093-0402, USA

Abstract

Mean-flow effects are discussed for two different pattern-forming systems: Rayleigh–Bénard convection and Faraday instability in viscous fluid. In both systems spirals are observed in certain parameter regions. In the Rayleigh–Bénard convection, the spiral-core instability is shown to occur due to the mean flow generated by the curved rolls near the core. In the Faraday instability, the mean flow which is generated by rapidly decaying surface waves near the wall, causes wave number frustration which leads to a rigid-body spiral rotation. In both cases we use phenomenological Swift–Hohenberg-type equations for the order parameter coupled to a large-scale mean flow. Numerical simulations are compared to recently reported experimental results. © 1998 Published by Elsevier Science B.V. All rights reserved.

1. Introduction

Nonlinear evolution of cellular patterns in extended systems near the threshold of a primary instability are usually studied using amplitude equations (e.g., Newell–Whitehead–Segel equation for roll patterns in isotropic systems [1,2]). These amplitude equations can be derived from the first principles by perturbative expansion using the supercriticality ε as a small parameter. However, the expansion is based on a pre-chosen orientation of the cellular pattern and thus do not preserve the full spatial symmetry of the physical system. Therefore, this description fails for more complicated patterns such as coexisting domains with varying orientation of rolls, targets, spirals, etc. To overcome this difficulty, phenomenological models similar to the so-called Swift–Hohenberg equation (SHE),

$$\partial_t \psi = \varepsilon \psi - (1 + \nabla^2)^2 \psi - \psi^3, \quad (1)$$

are often employed (see Ref. [3] and references therein). This model correctly describes the linear properties of the system close to the threshold and yet preserves the rotational

¹ Supported by the US DOE under contracts DE-FG03-95ER14516 and DE-FG03-96ER14592.

symmetry of the system. The disadvantage of this approach is that the nonlinear term in this equation is usually added ad hoc in order to provide a saturation of the primary instability and cannot be systematically derived from underlying first principles. Thus, while some of the features (including some secondary instabilities, domain coarsening, etc.) of the pattern formation can be modeled based on this equation, some other essential features of the dynamics may be missing. In many examples these features are related to the coupling between the cellular mode and so-called zero-mode slowly varying both in space and time. It can be a concentration field in binary-fluid convection [4], population inversion in extended lasers [5], density field in granular media [6], mean flow in Rayleigh–Bénard convection [7–9]. This problem can be rectified by expanding the basic model (Eq. (1)) so that it includes the interaction with the zero mode. It allows to reproduce many subtle features of the dynamics of cellular patterns within a simple phenomenological description.

In this paper we illustrate these general ideas by two examples of spiral dynamics in Rayleigh–Bénard convection and oscillating fluid layer. In both cases the spiral rotation is intimately related to the interaction with mean flow, self-generated by the cellular patterns in case of convection, and wall generated in case of Faraday system. We show that recently observed spiral-core instability [10–12] in Rayleigh–Bénard convection in Boussinesq fluid can be understood within the model for the order parameter coupled with the mean flow [13]. We also demonstrate that spiral rotation in Faraday experiment can be explained by the wave number frustration which is caused by the near-wall radial mean-flow generated by decaying capillary waves [14].

2. Spirals in Rayleigh–Bénard convection

Recently discovered spiral-defect chaos (SDC) in large aspect ratio Rayleigh–Bénard convection system at small Prandtl number [15,16] was successfully reproduced both within Navier–Stokes equations [17] and also using SHE coupled to the equation for the mean flow generated by the curved rolls [18],

$$\psi_t + (\mathbf{u} \cdot \nabla)\psi = \varepsilon\psi - g\psi^3 + 3(1-g)(\nabla\psi)^2\nabla^2\psi - (1+\nabla^2)^2\psi, \quad (2)$$

$$\Omega_t - \sigma(\nabla^2 - c^2)\Omega = g_m\hat{z} \cdot \nabla(\nabla^2\psi) \times \nabla\psi, \quad (3)$$

$$\Omega = \hat{z} \cdot \nabla \times \mathbf{u}. \quad (4)$$

Here ψ is the order parameter, \mathbf{u} the horizontal velocity field of the large-scale flow, and Ω the vertical component of the vorticity. The control parameter ε represents the reduced Rayleigh number, while σ characterizes the Prandtl number of the fluid. The parameter g allows to more accurately reproduce the stability properties of convection patterns [9], and g_m characterizes the coupling strength between the order parameter ψ and the vorticity Ω . The phenomenological parameter c is introduced to describe the local dissipation of the vorticity (e.g. due to friction at the bottom of the convection cell) [9,3]. Thus, Eq. (2) describes the dynamics of the order parameter ψ , while

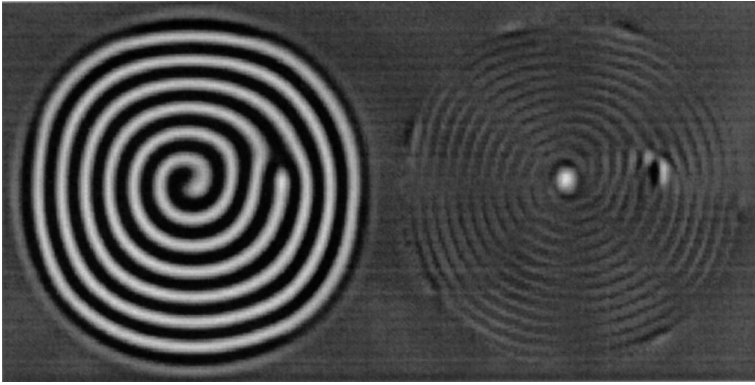


Fig. 1. Snapshot of the order-parameter ψ (left) and vorticity Ω (right) for a stationary rotating spiral terminated by a dislocation for Eqs. (2)–(4) with $\varepsilon = 0.7$, $g = 1$, $g_m = 50$, $c^2 = 2$, and $\sigma = 1$.

Eq. (3), using the definition of the vorticity (Eq. (4)), represents the coupling of the large-scale flow field \mathbf{u} and the order parameter. For $g = 1$ and $g_m = 0$, Eqs. (2)–(4) reduce to the Swift–Hohenberg equation, Eq. (1). We solved Eqs. (2)–(4) numerically in a domain of 256×256 collocation points using a pseudo-spectral method based on the fast Fourier transform. The physical domain size was typically restricted to 150×150 . Circular boundary conditions were enforced by ramping ε towards negative values at distances from the center $r > R_{\max} = 55$.

Essential features of SDC include spontaneous spiral creation, quasi-stationary spiral rotation, spiral-core instability, and eventual spiral destruction by other spirals. Cross and Tu [19] showed that persistent spiral rotation is caused by the wave-number frustration between the values selected by the spiral core and by the environment (most typically, roll dislocations). It is noteworthy that large vorticity generated in the spiral core plays only the secondary role in this mechanism since the asymptotic wave number selected by the core does not depend on the Prandtl number and coupling to the mean flow (parameter g_m in Eq. (3)). However, vorticity plays a major role in wave-number selection by the roll dislocation. It is easy to see that the dislocation in the roll pattern generates a vortex pair which drives the dislocation towards the half-plane with greater wave number (see Fig. 1 where the order parameter for individual spiral terminated by a dislocation is shown together with corresponding mean-flow vorticity). At small $g_m \varepsilon$ the dislocation climbing speed due to vorticity is $v \propto g_m \varepsilon$. The dislocation is stationary when this mean-flow drift is balanced by the ordinary climbing velocity $v_c \propto (1 - q_d)^{3/2}$ [20], therefore the selected wave number $q_{d0} \propto 1 - \alpha(g_m \varepsilon)^{2/3}$ (α is a constant depending on other parameters g, σ, c). In a stationary rotating spiral, wave number q_d near the dislocation is larger than q_{d0} so the dislocation moves around the core of the spiral with an angular velocity coinciding with the frequency of the core rotation. It is easy to see from the phase-diffusion equation (see Ref. [19]) that the frequency of the spiral rotation is inversely proportional to the distance from the core to dislocation. Detailed measurements of individual spiral rotation rate confirms this prediction [21].

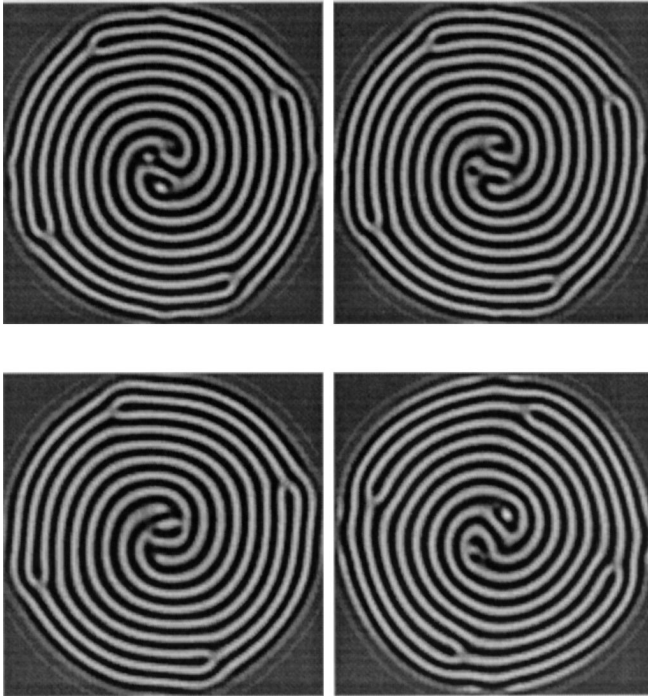


Fig. 2. A sequence of snapshots of the order parameter for a four-arm spiral with core oscillations for Eqs. (2)–(4) with $\varepsilon = 0.5$, $g = 1$, $g_m = 50$, $c^2 = 1$, and $\sigma = 1$.

At large supercriticality, a novel instability of the spiral core was recently observed [10–12]. The core exhibits high-frequency oscillations (with a period of several vertical diffusion times as compared with a period of overall spiral rotation of a few hundred vertical diffusion times). Using phase approximation (see Refs. [3,19]) it is easy to see that this instability is caused by the large-vorticity generated near the core of the spiral. Indeed, in the phase approximation, outside the core of the spiral the phase is described by

$$\theta_t + \mathbf{U} \cdot \nabla \theta = \tau(q)^{-1} \nabla \cdot [\mathbf{q}B(q)], \quad (5)$$

where $\tau(q)$, $B(q)$ are known functions of the wave number $\mathbf{q} = \nabla \theta$ ($B(1) = 0$, $B(q_d) < 0$ for SHE), see Ref. [3]. For stationary rotating n -armed spiral, $\theta = \int q(r) dr + n\phi - \omega t$, and therefore local wave number $q(r)$ obeys the following ODE:

$$\omega = -\frac{\Gamma}{r^2} - \tau(q)^{-1} \frac{d}{dr} [qB(q)], \quad (6)$$

where Γ is a total circulation of the mean flow around the spiral core. It is easy to see that for $1 - q_d \ll 1$ the wave number $q(r) \approx 1 - A_1 r - A_2 n \Gamma / r^2$, where $A_{1,2}$ are constants depending on τ and B . The wave number slowly rises towards the core and then rapidly decreases in its near vicinity. Of course, this expression is only valid outside the core

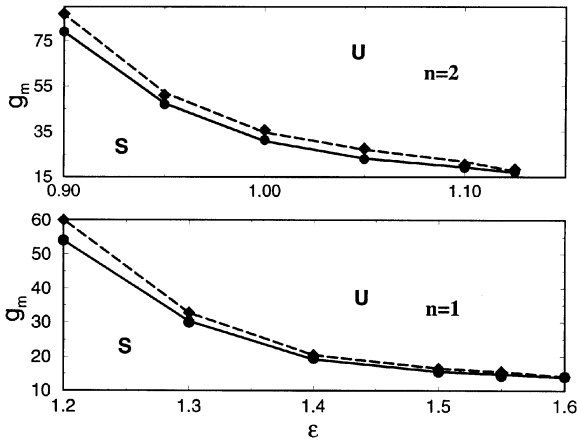


Fig. 3. Stability diagram for one- (a) and two-armed (b) spirals for $c^2 = 2$, $\sigma = 1$ and $g = 1$. As ϵ increases, the spiral-core becomes unstable at the dashed line, regaining stability at the solid line as ϵ decreases (from [13]).

of the dislocation ($r > 1$), however, it illustrates the tendency for the core vortex to locally unwind the spiral. If Γ gets large, the wave number near the core goes outside the stability balloon and the spiral-core becomes unstable. Visually, it appears as that the core rotates against the overall spiral rotation (see a series of snapshots in Fig. 2 and computer movie at <http://inls.ucsd.edu/~lev/conv/>). This behavior is qualitatively similar to that observed in a recent experiment by Plapp and Bodenschatz [10]. The threshold of this core instability depends on both ϵ and g_m as well as the topological charge n , see Fig. 3.

3. Spirals in a Faraday system

Parametric instability of a flat fluid surface subject to vertical oscillations remains a popular experimental tool for various pattern-formation phenomena. Squares, rolls, hexagons and higher-order quasi-patterns have been observed in different regions of parameters (viscosity, driving frequency, and depth of the fluid layer). Phase diagram of different patterns has been recently computed by Chen and Viñals based on the Navier–Stokes equations [22]. In the region of large viscosity and large h/λ , straight rolls are a stable pattern. However, as in case of Rayleigh–Bénard convection, stable rotating spirals have been recently observed in the same parameter region [23,14]. In this section we discuss the origin of the spiral rotation within the order-parameter model for the parametric instability

$$\frac{\partial \psi}{\partial t} = \gamma \psi * -v \psi - (1 + i\alpha)|\psi|^2 \psi + i\kappa(\nabla^2 + 1)\psi - (\mathbf{u} \cdot \nabla)\psi. \tag{7}$$

Here ψ is a complex amplitude of surface oscillations at the parametric frequency ω_0 (which is a half of the driving frequency), γ a forcing magnitude, κ the dispersion

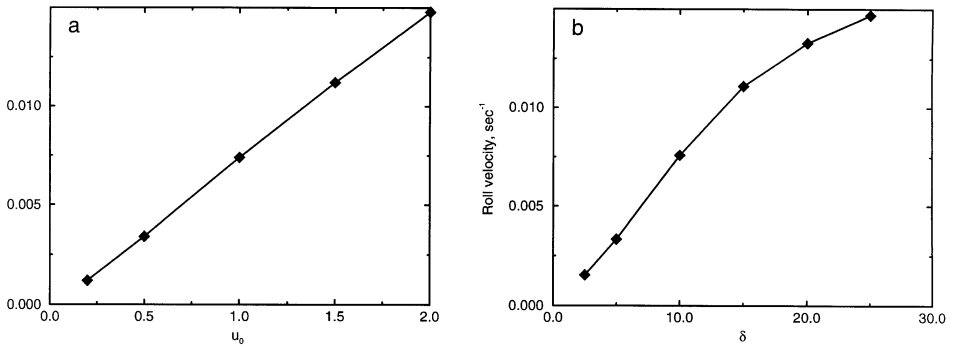


Fig. 4. Phase velocity of waves as a function of near-wall flow magnitude u_0 (a) and inverse scale ξ (b) from numerical simulations of Eq. (7). Parameters of simulations: $\gamma = 1.0$, $\nu = 0.5$, $\alpha = 0.0$, $\kappa = 1.0$, $k_0 = 1$, $\xi = 0.1$. In a, $\xi = 0.1$, in b, $u_0 = 1.0$ (from [14]).

parameter, and \mathbf{u} the velocity of the mean flow. Linear terms in this equation can be derived from the dispersion relation for capillary waves under parametric excitation, expanded near $\omega = \omega_0$, $q = 1$. The nonlinear term cannot be derived rigorously, as in Eq. (2) for Rayleigh–Bénard convection, and has been added ad hoc to account for the stabilization of the parametric instability. Imaginary part of the nonlinear coefficient α describes nonlinear frequency shift (see also Ref. [24]).

The last term in the r.h.s. of Eq. (7) describes order-parameter advection by the mean flow. Such mean flow was observed in experiments [14] near the walls of the cavity. This flow is caused by the momentum transfer from dissipating capillary waves at the driving frequency which are generated by oscillating side walls. This flow is directed off the walls near the surface and due to incompressibility returns back to the walls near the bottom. Velocity \mathbf{u} in Eq. (7) should be understood as an the average velocity over layer thickness weighted with the vertical structure of waves. Since surface waves decay towards the bottom, near-surface flow affects them stronger than near-bottom return flow and the net \mathbf{u} is oriented towards the center of the cavity.

Eq. (7) with periodic boundary conditions was studied numerically using pseudo-spectral split-step method with 256×256 collocation points, domain size $d = 200$ and integration time step 0.05. To simulate waves in circular cavity, we ramped linear dissipation outside the circle of radius $r_0 = 86$, i.e. $\nu = \nu_0$, $r < r_0$ and $\nu = \nu_0(1 + k(r - r_0))$, $r > r_0$, where k varied between 0.5 and 1.0. We assumed that the flow had radial direction and was azimuthally symmetric, $\mathbf{u} = u(r)\hat{\mathbf{r}}$. We used the following profile for flow velocity, $u(r) = u_0 \exp[\xi(r - r_0)]$. For $\gamma > \nu$ trivial state is unstable with respect to perturbations with wave numbers near 1. Numerical simulations show that at the nonlinear stage, these perturbations give rise to various cellular patterns, including plane waves, targets and spirals. Without mean-flow term ($u_0 = 0$), these patterns remain stationary even when nonlinear coefficient in Eq. (7) is complex. Nonlinear frequency shift $\propto \alpha$ only leads to deviation of the selected wave number from $q = 1$. (In systems with ordinary (nonparametric) pattern-forming instabilities nonpotential effects usually

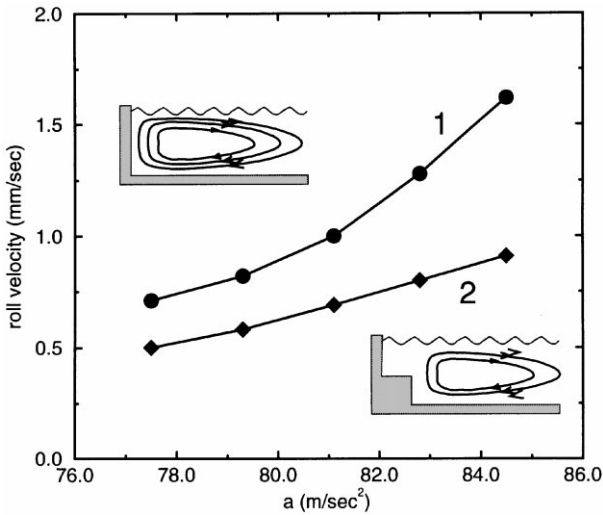


Fig. 5. Velocity of wave drift (measured by nodes displacement) as a function of magnitude of vertical acceleration for two different profiles of side walls. Inset: Sketches of the vertical profiles of the side wall and the structure of the shear flow (from [14]).

lead to wave propagation.) However, when the near-wall flow is introduced in Eq. (7), standing-waves comprising targets and spirals begin to drift slowly toward the center. Fig. 4 shows rolls velocity as a function of u_0 and ξ . Note that $\xi \gg r_0^{-1}$ so the flow is absent in the bulk, still rolls are moving throughout the integration domain. The phase velocity of rolls grows linearly with u_0 as it should be expected.

This phenomenology can be understood in terms of the phase diffusion equation similar to Eq. (5) for Rayleigh–Bénard system. The important difference is that here we have standing waves, and therefore two phases θ_+ and θ_- should be introduced. However, for large parametric forcing, the sum of phases $\theta_+ + \theta_-$ is slaved to the phase difference $\Theta = \theta_+ - \theta_-$. The equation for the latter reads

$$\partial_t \Theta + \mathbf{U} \cdot \nabla \Theta = \tau^{-1}(q) \nabla \cdot [\mathbf{q} B(q)], \tag{8}$$

where $\mathbf{q} = \frac{1}{2} \nabla \Theta$ and $\tau(q), B(q)$ are functions of the wave number q . For the spiral, $\theta_{\pm} = \pm(\int q dr + m\phi) - \omega_{\pm} t$. Multiplying Eq. (8) by $\tau(q)$ and integrating from $r = 0$ to R_{\max} we obtain

$$\omega_s \int \tau(q) dr = - \int U(r) q \tau(q) dr + q B(q)|_{r=R_{\max}}, \tag{9}$$

where $\omega_s = \omega_- - \omega_+$ is a frequency of spiral rotation. For $q \approx 1$ the last term in Eq. (9) is small and the frequency of spiral rotation can be estimated as $\omega_s \propto \int U(r) dr \approx u_0 \xi^{-1}$. This relation is in an agreement with numerical simulations (see Fig. 4).

The mechanism of spiral rotation which we described is based on the assumption that the radial flow is produced by the rapidly decaying waves near the wall generated by the oscillating meniscus. If this hypothesis is correct, the phase velocity of waves

should increase linearly with the magnitude of driving. It also should depend sensitively on the wall profile. Indeed, experiments [14] confirmed this prediction (see Fig. 5).

4. Conclusions

In this paper we briefly considered two different pattern-forming systems within the framework of order-parameter models coupled with mean flow. It turned out that both for Rayleigh–Bénard convection and Faraday system the mean flow plays a crucial role for spiral dynamics. In the former, vortex-pairs generated by roll dislocations, move the selected wave number away from the value selected by the spiral core and lead to wave-number frustration. The frustration in turn leads to the persistent spiral rotation. The strong vortex which is generated in the core of the spiral plays a minor role in the overall spiral rotation, however, it leads to the local spiral unwinding and eventually to the spiral-core instability.

In the Faraday system, stable rotating spirals have been recently observed. We showed that rotation of these spirals is caused by the near-wall radial flow which leads to the wave number frustration in the bulk. This near-wall flow is generated by rapidly decaying meniscus waves at the driving frequency.

The results presented in this paper have been obtained in collaboration with I. Aranson, M. Assenheimer, and V. Steinberg (Rayleigh–Bénard convection) and S.V. Kiyashko, L.N. Korzinov, and M.I. Rabinovich (Faraday system).

References

- [1] A.C. Newell, J.A. Whitehead, *J. Fluid. Mech.* 38 (1969) 279.
- [2] L.A. Segel, *J. Fluid Mech.* 38 (1969) 203.
- [3] M. Cross, P.C. Hohenberg, *Rev. Mod. Phys.* 65 (1993) 851.
- [4] H. Riecke, *Physica D* 61 (1992) 253.
- [5] J. Lega, J.V. Moloney, A.C. Newell, *Phys. Rev. Lett.* 73 (1994) 2978.
- [6] L.S. Tsimring, I. Aranson, *Phys. Rev. Lett.* 79 (1997) 213.
- [7] E. Siggia, A. Zippelius, *Phys. Rev. Lett.* 47 (1981) 835.
- [8] P. Manneville, *J. Phys. (Paris)* 44 (1983) 563.
- [9] H.S. Greenside, M.C. Cross, *Phys. Rev. A* 31 (1985) 2492.
- [10] B.B. Plapp, E. Bodenschatz, Core dynamics of multi-armed spirals in Rayleigh–Bénard convection, *Phys. Scripta T* 67 (1996) 111.
- [11] M. Assenheimer, V. Steinberg, *Phys. Rev. Lett.* 76 (1996) 756.
- [12] M. Assenheimer, Ph.D. Thesis, 1996.
- [13] M. Assenheimer, I. Aranson, V. Steinberg, L.S. Tsimring, *Phys. Rev. E* 55 (1997) R4877.
- [14] S.V. Kiyashko, L.N. Korzinov, M.I. Rabinovich, L.S. Tsimring, *Phys. Rev. E* 54 (1996) 5037.
- [15] S.W. Morris, E. Bodenschatz, D.S. Cannell, G. Ahlers, *Phys. Rev. Lett.* 71 (1993) 2026.
- [16] M. Assenheimer, V. Steinberg, *Phys. Rev. Lett.* 70 (1993) 3888.
- [17] W. Decker, W. Pesch, A. Weber, *Phys. Rev. Lett.* 73 (1994) 648.
- [18] H. Xi, J.D. Gunton, J. Viñals, *Phys. Rev. Lett.* 71 (1993) 2030.
- [19] M.C. Cross, Y. Tu, *Phys. Rev. Lett.* 73 (1995) 834.
- [20] E. Siggia, A. Zippelius, *Phys. Rev. A* 24 (1981) 1036.

- [21] E. Bodenschatz, Report at the APS Meeting, Kansas City, March 1997.
- [22] P. Chen, J. Viñals, *Phys. Rev. Lett.* 79 (1997) 2670.
- [23] W.S. Edwards, S. Fauve, *J. Fluid. Mech.* 278 (1994) 123.
- [24] W. Zhang, J. Viñals, *Phys. Rev. Lett.* 74 (1995) 690.